Induced Superconductivity in the Quantum Spin Hall Edge

Induced Superconductivity in the Quantum Spin Hall Edge

Sean Hart[†1], Hechen Ren[†1], Timo Wagner[1], Philipp Leubner[2], Mathias Mühlbauer[2], Christoph Brüne[2], Hartmut Buhmann[2], Laurens W. Molenkamp[2], Amir Yacoby[1]

[1]Department of Physics, Harvard University, Cambridge, MA, USA

[2] Physikalisches Institut (EP3), Universität Würzburg, 97074 Würzburg, Germany

[†]These authors contributed equally to this work

Abstract

Topological insulators are a newly discovered phase of matter characterized by a gapped bulk surrounded by novel conducting boundary states [1, 2, 3]. Since their theoretical discovery, these materials have encouraged intense efforts to study their properties and capabilities. Among the most striking results of this activity are proposals to engineer a new variety of superconductor at the surfaces of topological insulators [4, 5]. These topological superconductors would be capable of supporting localized Majorana fermions, particles whose braiding properties have been proposed as the basis of a fault-tolerant quantum computer [6]. Despite the clear theoretical motivation, a conclusive realization of topological superconductivity remains an outstanding experimental goal. Here we present measurements of superconductivity induced in two-dimensional HgTe/HgCdTe quantum wells, a material which becomes a quantum spin Hall insulator when the well width exceeds $d_C = 6.3$ nm [7]. In wells that are 7.5 nm wide, we find that supercurrents are confined to the one-dimensional sample edges as the bulk density is depleted. However, when the well width is decreased to 4.5 nm the edge supercurrents cannot be distinguished from those in the bulk. These results provide evidence for superconductivity induced in the helical edges of the quantum spin Hall effect, a promising step toward the demonstration of one-dimensional topological superconductivity. Our results also provide a direct measurement of the widths of these edge channels, which range from 180 nm to 408 nm.

Topological superconductors, like topological insulators, possess a bulk energy gap and gapless surface states. In a topological superconductor, the surface states are predicted to manifest as zero-energy Majorana fermions, fractionalized modes which pair to form conventional fermions. Due to their non-Abelian braiding statistics, achieving control of these Majorana modes is desirable both fundamentally and for

applications to quantum information processing. Proposals toward realizing Majorana fermions have focused on their emergence within fractional quantum Hall states [8] and spinless $p+ip$ superconductors [9], and on their direct engineering using s-wave superconductors combined with topological insulators or semiconductors [10, 11]. Particularly appealing are implementations in one-dimensional (1D) systems, where Majorana modes would be localized to the ends of a wire. In such a 1D system, restriction to a single spin degree of freedom combined with proximity to an s-wave superconductor would provide the basis for topological superconductivity [12]. Effort in this direction has been advanced by studies of nanowire systems [13, 14, 15, 16, 17, 18] and by excess current measurements on InAs/GaSb devices [19]. Given the wide interest in Majorana fermions in one dimension, it is essential to expand the search to other systems whose properties are suited toward their control.

An attractive route toward a 1D topological superconductor uses as its starting point the two-dimensional (2D) quantum spin Hall (QSH) insulator. This topological phase of matter was recently predicted [20, 21] and observed [22, 23] in HgTe/HgCdTe quantum wells thicker than a critical thickness $d_C = 6.3$ nm. Due to strong spin-orbit coupling the bulk bands of the system invert, crossing only at the edges of the system to form 1D counterpropagating helical modes. Time-reversal symmetry ensures protection of these modes against elastic backscattering over distances shorter than the coherence length [24]. The helical nature of the edge modes makes them a particularly appealing path toward the realization of a topological superconductor, due to the intrinsic elimination of their spin degree of freedom. Here we report measurements of supercurrents confined to edge states in HgTe/HgCdTe quantum well heterostructures, a critical step toward the demonstration of 1D topological superconductivity.

Our approach consists of a two-terminal Josephson junction, with a rectangular section of quantum well located between two superconducting leads (Figure 1). At a given bulk carrier density, the presence or absence of helical edge channels influences the supercurrent density profile across the width of the junction. In the simplest case the supercurrent density is uniform throughout the device, and edge channels are indistinguishable from bulk channels (Figure 1a). This behavior would be expected for a non-topological junction (quantum well width smaller than d_C), or in a topological junction (quantum well width larger than d_C) far from the bulk insulating regime.

In a topological junction, decreasing the bulk carrier density brings the device closer to the QSH insulator regime (Figure 1b). Scanning SQUID measurements suggest that over a range of bulk densities the QSH edge channels coexist with bulk states, and can carry considerably more edge current than would be expected for a non-topological conductor [25]. In the two-terminal configuration, this helical edge contribution appears as peaks in the supercurrent density at each edge. When the bulk density becomes sufficiently low, these edge peaks are the only features in the supercurrent density (Figure 1c).

Then the supercurrent is carried solely along the helical edges, and the system is in the regime of the quantum spin Hall superconductor.

Placing such a Josephson junction in a perpendicular magnetic field B provides a way to measure the supercurrent density in the quantum well. In general, the maximum supercurrent that can flow through a Josephson junction is periodically modulated by a magnetic field. Typically, the period of the modulation corresponds to the magnetic flux quantum $\Phi_0 = h/2e$. In our junctions this period matches the area of the HgTe region plus half the area occupied by each contact, a result of the Meissner effect. The particular shape of the critical current interference pattern depends on the phase-sensitive summation of the supercurrents traversing the junction [26]. In the case of a symmetric supercurrent distribution, this integral takes the simple form:

$$I_C^{max}(B) = \left| \int_{-\infty}^{\infty} dx J_S(x) \cos(2\pi L_J B x/\Phi_0) \right|.$$

Here L_J is the length of the junction along the direction of current, accounting for the magnetic flux focusing from the contacts.

It is evident that different supercurrent densities $J_S(x)$ in the junction can give rise to different interference patterns $I_C^{max}(B)$. The flat supercurrent density of a trivial conductor corresponds to a single-slit Fraunhofer pattern $|(\sin(\pi L_J B W/\Phi_0))/(\pi L_J B W/\Phi_0)|$, characterized by a central lobe width of $2\Phi_0$ and side lobes decaying with $1/B$ dependence (Figure 1a). As helical edges emerge, this single-slit interference evolves toward the more sinusoidal oscillation characteristic of a SQUID (Figure 1b). The central lobe width shrinks to Φ_0 when only edge supercurrents remain, with the side lobe decay determined by the widths of the edge channels (Figure 1c). Measuring the dependence of I_C^{max} on B therefore provides a convenient way to measure the distribution of supercurrent in a junction. To quantitatively extract $J_S(x)$ from the measured quantity $I_C^{max}(B)$ we follow an approach developed by Dynes and Fulton, where nonzero $I_C^{max}(B)$ minima are ascribed to an asymmetric supercurrent distribution [27]. Although other effects may lead to nonzero minima in $I_C^{max}(B)$, we consider here only the possibility of an odd component in $J_S(x)$. Full details of the extraction procedure can be found in the Supplementary Information.

To study how supercurrents flow in the QSH regime, we measure a Josephson junction consisting of a 7.5 nm-wide quantum well contacted by titanium/aluminum leads. Our contact lengths are each 1 μm, and the contact separation is 800 nm. The junction width of 4 μm is defined by etched mesa edges. A voltage V_G applied to a global topgate allows us to tune the carrier density in the junction. At each value of V_G and B, the critical current I_C^{max} is determined by increasing the current through the junction while monitoring the voltage across the leads. The behavior observed in this device is

reproducable in several other similar junctions, as reported in the Supplementary Information.

As a function of the topgate voltage, the overall behavior of the junction evolves between two extremes. At more positive gate voltage and higher bulk density, the critical current envelope strongly resembles a single-slit pattern (Figure 2a). This type of interference suggests a nearly uniform supercurrent density throughout the sample, confirmed by transformation to the $J_S(x)$ picture (Figure 2b). This nearly flat distribution indicates that the quantum well is in the high carrier density regime of an essentially trivial conductor.

At more negative gate voltage and lower bulk density, the critical current envelope becomes close to a sinusoidal oscillation (Figure 2c). The shift toward a SQUID-like interference pattern corresponds to the development of sharp peaks in supercurrent density at the mesa edges (Figure 2d).

We can track this evolution in a single device by measuring the critical current envelope at a series of gate voltages. As the topgate is varied from $V_G = 1.05$ V to $V_G = -0.45$ V, the maximum critical current decreases from 505 nA to 5.7 nA. At the same time, the overall critical current behavior shows a narrowing of the central interference lobe, from $2\Phi_0$ at positive gate voltages to Φ_0 at negative gate voltages (Figure 3a,b). The side lobes additionally become continuously more pronounced, indicating the confinement of supercurrent to channels at the edges of the junction (Figure 3c,d). The normal resistance, measured at large bias to overcome superconductivity, increases from 160 Ω to $\sim 3,000$ Ω over the range of this transition. While it is possible to gate further toward depletion, the critical currents become too small to reliably measure and no meaningful supercurrent density can be extracted.

At the most negative gate voltage, $V_G = -0.45$ V, we can estimate the widths of the supercurrent-carrying edge channels using a Gaussian lineshape (Figure 3f). Using this method, we find widths of 408 nm and 319 nm for the two edges. Our measurements of edge widths in another device with similar dimensions, as well as one with a 2 μm mesa width, show edges as narrow as 180 nm (see Supplementary Information). These width variations, as well as the normal state resistance that is low compared to the resistance $h/2e^2$ for two ballistic 1D channels, suggest the presence of additional edge modes or of bulk modes coupled too weakly across the junction to carry supercurrent.

To provide further evidence that the observed edge supercurrents are topological in nature, we next turn to a heterostructure with a quantum well width of 4.5 nm. In this device, the well width is smaller than the critical width d_C, so that the sample is not expected to enter the QSH regime. Near zero topgate voltage and a normal resistance of 270 Ω, the critical current interference pattern has a maximum of 243 nA and resembles a single-slit envelope (4a,b). Upon energizing the topgate and decreasing the bulk density, the single-slit pattern persists. In contrast to the wide well sample, this behavior corresponds to a supercurrent density that remains distributed throughout the junction even as the normal resistance

rises to several kΩ (Figure 4c-f). Because the edge supercurrents are present only when the well width is larger than d_C, we conclude that our observations provide evidence for induced superconductivity in the helical QSH edge states.

The ability to induce supercurrents through the helical edges of a two-dimensional topological insulator represents a significant step toward the realization of topological superconductivity. A one-dimensional system with superconducting pairing and only one spin degree of freedom should be capable of entering a topological phase, allowing Majorana zero-modes at its ends. The HgTe/HgCdTe system represents a natural host for these effects, since its edge modes occur in the same manner as the paired electrons of an s-wave superconductor. Our observation of supercurrents confined to the edges of topologically nontrivial HgTe quantum wells distinguishes this system as an especially promising platform in which to study the physics emerging from interactions among electrons in reduced dimensions.

References

[1] Hasan, M. Z. & Kane, C. L. Colloquium: Topological insulators. *Reviews of Modern Physics* **82**, 3045–3067 (2010).

[2] Qi, X.-L. & Zhang, S.-C. Topological insulators and superconductors. *Reviews of Modern Physics* **83**, 1057–1110 (2011).

[3] Kane, C. L. & Mele, E. J. Z2 topological order and the quantum spin hall effect. *Physical Review Letters* **95**, 146802 (2005).

[4] Fu, L. & Kane, C. L. Superconducting proximity effect and majorana fermions at the surface of a topological insulator. *Physical Review Letters* **100**, 096407 (2008).

[5] Fu, L. & Kane, C. L. Josephson current and noise at a superconductor/quantum-spin-hall-insulator/superconductor junction. *Physical Review B* **79**, 161408 (2009).

[6] Nayak, C. *et al.* Non-abelian anyons and topological quantum computation. *Reviews of Modern Physics* **80**, 1083–1159 (2008).

[7] Konig, M. *et al.* The quantum spin hall effect: Theory and experiment. *Journal of the Physical Society of Japan* **77, No. 3**, 031007 (2008).

[8] Moore, G. & Read, N. Nonabelions in the fractional quantum hall effect. *Nuclear Physics B* **360**, 362–396 (1991).

[9] Read, N. & Green, D. Paired states of fermions in two dimensions with breaking of parity and time-reversal symmetries and the fractional quantum hall effect. *Physical Review B* **61**, 10267–10297 (2000).

[10] Jay D. Sau, S. T., Roman M. Lutchyn & Sarma, S. D. Generic new platform for topological quantum computation using semiconductor heterostructures. *Physical Review Letters* **104**, 040502 (2010).

[11] Alicea, J. Majorana fermions in a tunable semiconductor device. *Physical Review B* **81**, 125318 (2010).

[12] Kitaev, A. Y. Unpaired majorana fermions in quantum wires. *Physics-Uspekhi* **44**, 131 (2001).

[13] Mourik, V. *et al.* Signatures of majorana fermions in hybrid superconductor-semiconductor nanowire devices. *Science* **336**, 1003–1007 (2012).

[14] Das, A. *et al.* Zero-bias peaks and splitting in al-inas nanowire topological superconductor as a signature of majorana fermions. *Nature Physics* **8**, 887–895 (2012).

[15] Leonid P. Rokhinson, X. L. & Furdyna, J. K. The fractional a.c. josephson effect in a semiconductor-superconductor nanowire as a signature of majorana particles. *Nature Physics* **8**, 795–799 (2012).

[16] Lee, E. J. H. *et al.* Zero-bias anomaly in a nanowire quantum dot coupled to superconductors. *Physical Review Letters* **109**, 186802 (2012).

[17] Churchill, H. O. H. *et al.* Superconductor-nanowire devices from tunneling to the multichannel regime: zero-bias oscillations and magnetoconductance crossover. *Physical Review B* **87**, 241401(R) (2013).

[18] Finck, A. D. K. *et al.* Anomalous modulation of a zero-bias peak in a hybrid nanowire-superconductor device. *Physical Review Letters* **110**, 126406 (2013).

[19] Ivan Knez, G. S., Rui-Rui Du. Andreev reflection of helical edge modes in inas/gasb quantum spin hall insulator. *Physical Review Letters* **109**, 186603 (2012).

[20] Bernevig, B. A. & Zhang, S.-C. Quantum spin hall effect. *Physical Review Letters* **96**, 106802 (2006).

[21] B. Andrei Bernevig, S.-C. Z., Taylor L. Hughes. Quantum spin hall effect and topological phase transition in hgte quantum wells. *Science* **314**, 1757–1761 (2006).

[22] Konig, M. *et al.* Quantum spin hall insulator state in hgte quantum wells. *Science* **318**, 766–770 (2007).

[23] Roth, A. *et al.* Nonlocal transport in the quantum spin hall state. *Science* **325**, 294–297 (2009).

[24] Thomas L. Schmidt, F. v. O., Stephan Rachel & Glazman, L. I. Inelastic electron backscattering in a generic helical edge channel. *Physical Review Letters* **108**, 156402 (2012).

[25] Nowack, K. C. *et al.* Imaging currents in hgte quantum wells in the quantum spin hall regime. *Nature Materials* **Advance Online Publication** (2013).

[26] Tinkham, M. *Introduction to Superconductivity* (Dover Publications, Inc., 2004).

[27] Dynes, R. C. & Fulton, T. A. Supercurrent density distribution in josephson junctions. *Physical Review B: Condensed Matter and Materials Physics* **3, Number 9**, 3015–3023 (1971).

Acknowledgments: We acknowledge Anton Akhmerov and Jay Deep Sau for theoretical discussions. We acknowledge financial support from Microsoft Corporation Project Q, the NSF DMR-1206016, the DOE SCGF Program, the German Research Foundation (DFG-JST joint research program "Topological Electronics"), and EU ERC-AG program (project 3-TOP).

Author Contributions: All authors contributed collaboratively to the work.

Author Information: The authors declare no competing financial interests. Correspondence and requests for materials should be addressed to yacoby@physics.harvard.edu.

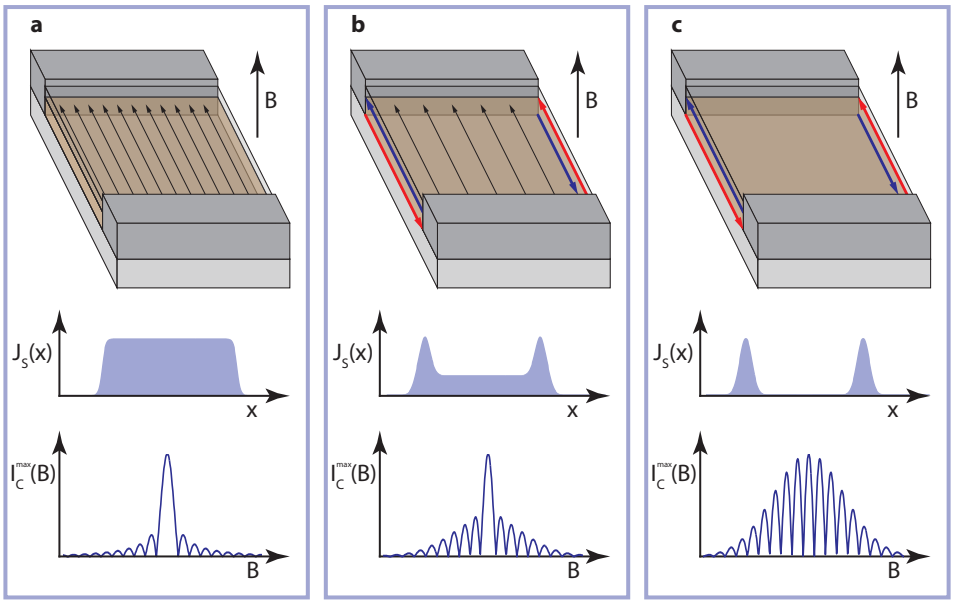

Figure 1: Expected two-terminal behavior in different regimes of a topological quantum well. a, When the bulk of a sample is filled with charge carriers, supercurrent can flow uniformly across the junction, corresponding to a flat supercurrent density $J_S(x)$. A perpendicular magnetic field B modulates the maximum critical current I_C^{max}, resulting in a single-slit Fraunhofer interference pattern. b, As the bulk carriers are depleted, the supercurrent density develops peaks due to the presence of the helical edges. This evolution toward edge-dominated transport appears in the interference pattern as a narrowing central lobe width and more pronounced side lobe amplitudes. c, When no bulk carriers remain, the supercurrent is carried only along the helical edges. In this regime the interference results in a sinusoidal double-slit pattern, with an overall decay in B that is determined by the width of the edge channels.

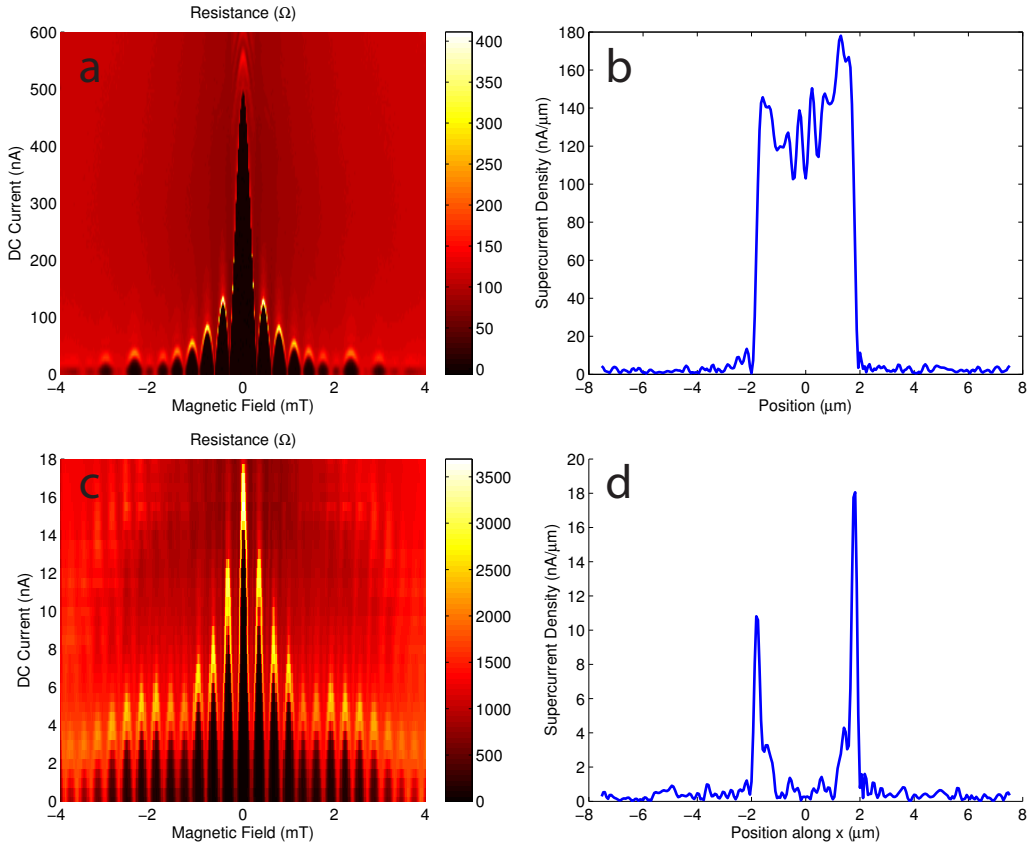

Figure 2: General behavior observed in the topological Josephson junction. a, A map of the differential resistance across the junction, measured with the topgate at $V_G = 1.05$ V, shows the single-slit interference characteristic of a uniform supercurrent density. b, The supercurrent density, extracted for $V_G = 1.05$ V, is consistent with trivial charge transport throughout the bulk of the junction. c, When the topgate voltage is lowered to $V_G = -0.425$ V, the differential resistance shows a more sinusoidal interference pattern. d, Using the inteference envelope measured at $V_G = -0.425$ V, the supercurrent density is clearly dominated by the contribution from the edges. In this regime almost no supercurrent passes through the bulk.

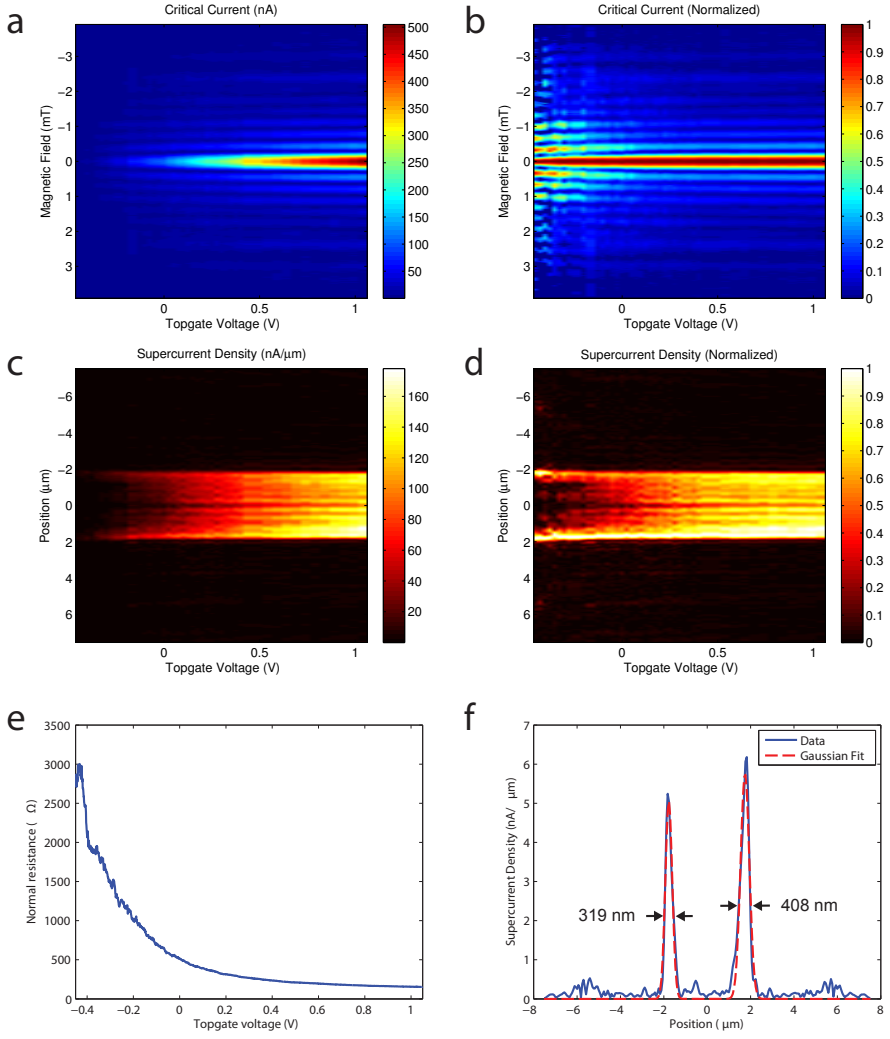

Figure 3: Continuous evolution with gating in the topological Josephson junction. a, As the topgate is varied from $V_G = 1.05$ V to $V_G = -0.45$ V, the maximum critical current decreases from 505 nA to 5.7 nA. b, Normalizing the interference patterns to their peak values reveals the evolution toward sinusoidal interference. c, Using the envelope at each gate voltage, the evolution of the supercurrent density can be visualized. d, By normalizing each supercurrent density to its maximum value, the transition from trivial to edge-dominated supercurrent transport can be clearly seen. e, This transition occurs as the normal device resistance increases from 160 Ω to 3,000 Ω. f, At the most negative gate voltage, $V_G = -0.45$ V, the supercurrent density provides a measurement of the edge widths.

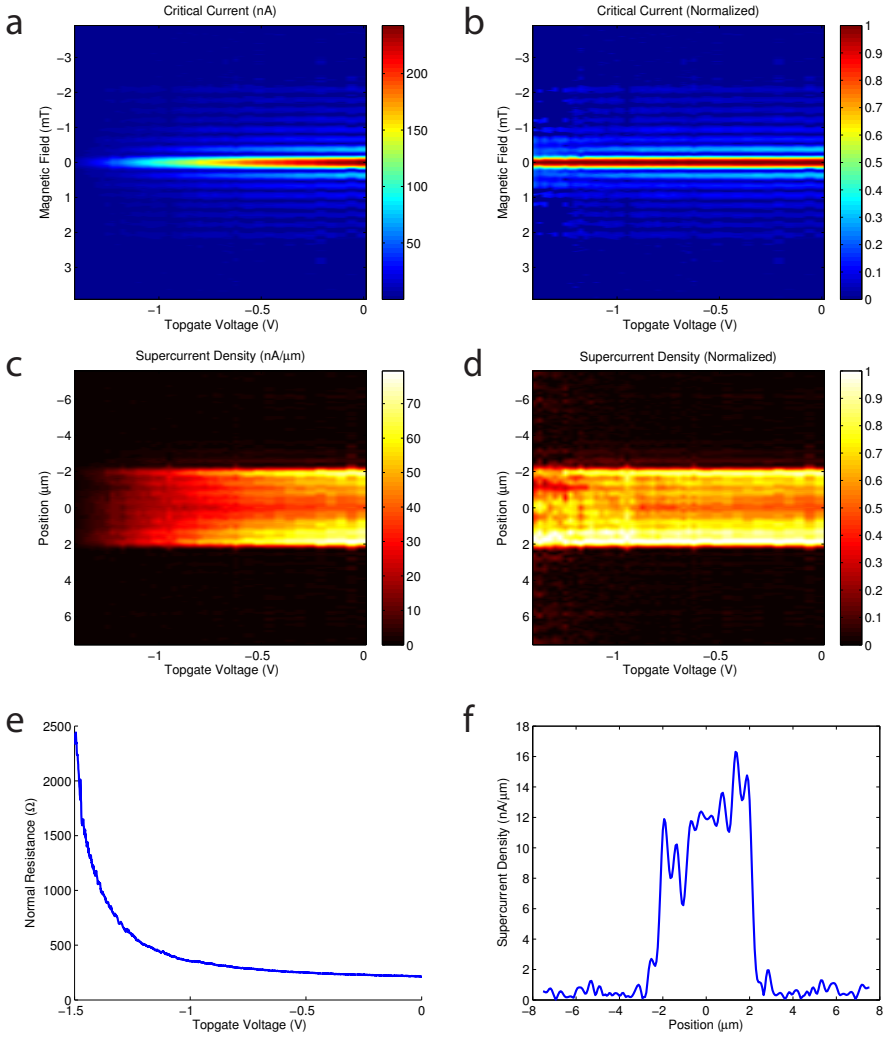

Figure 4: Continuous evolution with gating in the non-topological Josephson junction. a, As the topgate is varied from $V_G = 0$ V to $V_G = -1.5$ V, the maximum critical current decreases from 243 nA to 4.4 nA. b, Normalizing the interference patterns to their peak values shows the stability of the single-slit pattern over a wide range of gating. c, Using the envelope at each gate voltage, the evolution of the supercurrent density can be visualized. d, Normalizing each supercurrent density to its maximum value shows that the supercurrent remains distributed throughout the device. e, This roughly uniform supercurrent distribution remains even as the device resistance increases from 215 Ω to almost 2,500 Ω. f, A linetrace of the supercurrent density close to depletion further demonstrates that the supercurrent flows throughout the device.

Supplementary Information for Induced Superconductivity in the Quantum Spin Hall Edge

Sean Hart[†1], Hechen Ren[†1], Timo Wagner[1], Philipp Leubner[2], Mathias Mühlbauer[2], Christoph Brüne[2], Hartmut Buhmann[2], Laurens W. Molenkamp[2], Amir Yacoby[1]

[1]Department of Physics, Harvard University, Cambridge, MA, USA

[2] Physikalisches Institut (EP3), Universität Würzburg, 97074 Würzburg, Germany

[†]These authors contributed equally to this work

Device characteristics

Devices were fabricated on two different HgTe/HgCdTe heterostructures, with layer structures shown in Supplementary Figure 1. Wafer I contained a 7.5 nm quantum well with an electron density of $3.6 \times 10^{11}/\text{cm}^2$ and a mobility of $300,000$ cm^2/Vs. Wafer II contained a 4.5 nm quantum well with an electron density of $3.5 \times 10^{11}/\text{cm}^2$ and a mobility of $100,000$ cm^2/Vs.

Device processing consisted of the following steps. Mesas were defined by etching with an Ar ion source, and were 100 nm in height. Contacts consisted of 10 nm of titanium under 180 nm of aluminum, deposited by thermal evaporation after in situ cleaning with an Ar ion source. A 50 nm layer of aluminum oxide deposited by atomic layer deposition isolated the mesa and contacts from the topgate, which consisted of 10 nm of titanium under 250 nm of gold. An SEM image of a junction is depicted in Supplementary Figure 2.

Critical current measurement

Measurements were performed in a dilution refrigerator with a base temperature of 10 mK, and an electron temperature of 20 mK measured using standard Coulomb blockade techniques. At each voltage V_G on the topgate, the magnetic field was stepped through $B = 0$ mT over a range of 8 mT. At each value of magnetic field, the DC current I_{DC} through a junction was then increased while monitoring the DC voltage drop V_{DC} across the junction. A voltage threshold was used to determine the critical current; the point beyond which V_{DC} was increasing and above the threshold voltage was recorded as the critical current $I_C^{max}(B, V_G)$. Our threshold was set at 1 μV, several standard deviations above the noise level. There is an artificial offset introduced by this method when the critical current falls to

zero. In our analysis these artificial offset currents are reported as zero instead of the value given by the threshold method.

Analysis of current density profile

In a Josephson junction immersed in a perpendicular magnetic field B, the magnitude of the maximum critical current $I_C^{max}(B)$ depends strongly on the supercurrent density between the leads. For example, a uniform supercurrent density generates single-slit Fraunhofer interference, while a sinusoidal double-slit interference pattern arises from two supercurrent channels enclosing the junction area. In the following discussion we elaborate on this correspondence, outlining the quantitative way in which we convert our measured interference patterns to their originating supercurrent density profiles. We assume throughout that the current density varies only along the x direction, and that the supercurrent is directed along the orthogonal y direction. The junction then has a length L in the y direction, and the leads each have a length L_{Al}. Our method follows the approach developed by Dynes and Fulton [27].

At a fixed magnetic field, the total critical current through the Josephson junction is a phase-sensitive summation of supercurrent over the width of the junction. Suppose we have a supercurrent density profile $J_S(x)$. Then its complex Fourier transform yields a complex critical current function $\mathscr{I}_C(\beta)$,

$$\mathscr{I}_C(\beta) = \int_{-\infty}^{\infty} dx J_S(x) e^{i\beta x}, \tag{1}$$

where the normalized magnetic field unit $\beta = 2\pi(L + L_{Al})B/\Phi_0$, and the magnetic flux quantum $\Phi_0 = h/2e$.

The experimentally observed $I_C^{max}(\beta)$ is the magnitude of this summation: $I_C^{max}(\beta) = |\mathscr{I}_C(\beta)|$. Therefore to extract the supercurrent density from $I_C^{max}(\beta)$ it is necessary to first recover the complex critical current $\mathscr{I}_C(\beta)$.

This reduces to a particularly simple problem in the case of an even current density, $J_E(x)$, representing a symmetric distribution. The odd part of $e^{i\beta x}$ vanishes from the integral, and equation (1) becomes $\mathscr{I}_C(\beta) = I_E = \int_{-\infty}^{\infty} dx J_E(x) \cos\beta x$. Since $J_E(x)$ is real and positive, we see that $\mathscr{I}_C(\beta)$ is also real, and it typically alternates between positive and negative values at each zero-crossing. Because $I_C^{max}(\beta) = |\mathscr{I}_C(\beta)|$, we can therefore recover the exact $\mathscr{I}_C(\beta)$ by flipping the sign of every other lobe of the observed $I_C^{max}(\beta)$.

Now suppose that on top of this even function, the current distribution has a small but non-vanishing

odd component, $J_O(x)$, with its Fourier transform $I_O(\beta) = \int_{-\infty}^{\infty} dx J_O(x) \sin \beta x$. Then (1) gives

$$\mathscr{I}_C(\beta) = I_E(\beta) + iI_O(\beta). \tag{2}$$

The observed critical current $I_C^{max}(\beta) = \sqrt{I_E^2(\beta) + I_O^2(\beta)}$ is therefore dominated by $I_E(\beta)$ except at its minima points. Approximately, $I_E(\beta)$ is obtained by multiplying $I_C^{max}(\beta)$ with a flipping function that switches sign between adjacent lobes of the envelope function (Supplementary Figures 3,4a). When $I_E(\beta)$ is minimal, the odd part $I_O(\beta)$ dominates the critical current. $I_O(\beta)$ can then be approximated by interpolating between the minima of $I_C^{max}(\beta)$, and flipping sign between lobes (Supplementary Figure 4b). A Fourier transform of the resulting complex $\mathscr{I}_C(\beta)$, over the sampling range b of β, yields the current density profile (Supplementary Figure 5):

$$J_S(x) = \left| \frac{1}{2\pi} \int_{-b/2}^{b/2} d\beta \mathscr{I}_C(\beta) e^{-i\beta x} \right|. \tag{3}$$

Gating of resistance and supercurrent

To study the variation of the normal resistance as a function of the bulk carrier density, we swept the topgate voltage in the topological junction (main text) from $V_G = 1.05$ V to $V_G = -3$ V. Over this gate range, the differential resistance was measured using an AC excitation of 5 nA. We additionally maintained a constant DC voltage bias of 750 μV across the junction to avoid features related to superconductivity. The resulting normal resistance measurement displays two relatively conductive regimes separated by a resistance plateau peaking near 6-8 kΩ (Supplementary Figure 6a). This behavior is consistent with previous transport measurements of the QSH effect, where the QSH insulator state appears as a resistance peak when samples are gated from n-type to p-type regimes [22]. The value of the resistance plateau is lower than the expected resistance $h/2e^2$ for two ballistic 1D channels, suggesting that additional bulk modes are present. Near $V_G = -3$ V, our junction resistance saturates at 3 kΩ and we observe no superconductivity. This behavior can be explained by the formation of an n-p-n junction, where barriers between regions of different carrier type can block the transmission of supercurrent.

As we tune the topgate to more negative voltages, the maximum critical current of our junction decreases (Figure 3a). The electron temperature $T = 20$ mK provides an estimate $2ek_BT/\hbar \approx 1$ nA for the smallest critical currents that can still be reliably measured. For the topological junction shown in the main text (Figures 2, 3), this limit is reached above a topgate voltage of $V_G = -0.45$ V. However, even beyond this point clear magnetoresistance oscillations are still apparent. In Supplementary Figure

6b these oscillations are plotted for $V_G = -0.7$ V. The magnetic field period corresponds to the magnetic flux quantum $\Phi_0 = h/2e$ observed throughout the gating of the device, suggesting that supercurrent transport persists well into the QSH regime.

Additional devices

In addition to the two devices presented in the main text, we also measured several different junction geometries fabricated using the 7.5 nm quantum well heterostructure. One of these junctions had a width of 2 microns, but was otherwise identical to the topological device presented in the main text. This device also showed a transition from uniform bulk supercurrent to edge-dominated supercurrent, concurrently with the normal resistance rising from 300 ohms to 4,000 ohms (Supplementary Figure 7). The size of the magnetic field period in this device is 0.68 mT, consistent with the overall device area of 2 microns $\times$ (800 nm + 1 micron). From the supercurrent density profile in the QSH regime, we extract edge widths of 180 nm and 197 nm.

The other device, a 4 micron wide junction, was also identical to the topological junction from the main text except that the topgate was only 200 nm long and was threaded between the contacts. Although this topgate did not fully cover the junction, the behavior observed in this device was still consistent with the other topological devices (Supplementary Figure 8). This suggests that the gate effect was approximately uniform across the area between the contacts. When the normal resistance of the device was 4,000 ohms, supercurrent transport was observed in this device through edges with widths of 208 nm and 214 nm. Even after supercurrents became too small to measure, the normal resistance of this device approached the expected value of $h/2e^2$ for transport through two ballistic one-dimensional edge modes.

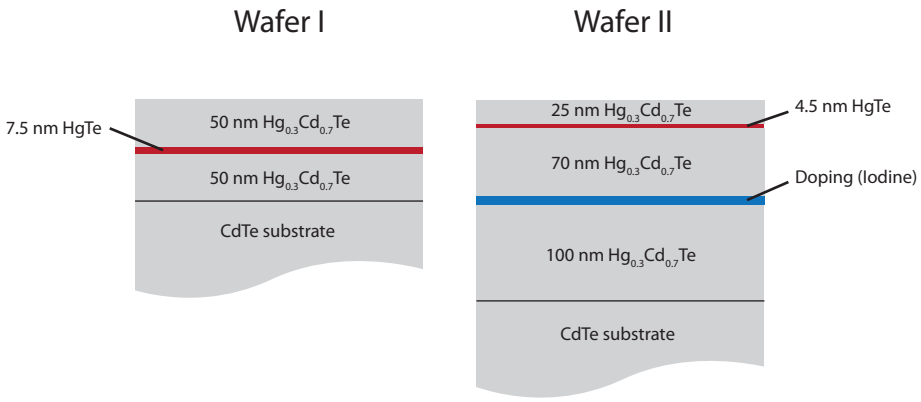

Supplementary Figure 1: Schematics of the heterostructures used in the experiment. The quantum well thicknesses were 7.5 nm for Wafer I and 4.5 nm for Wafer II.

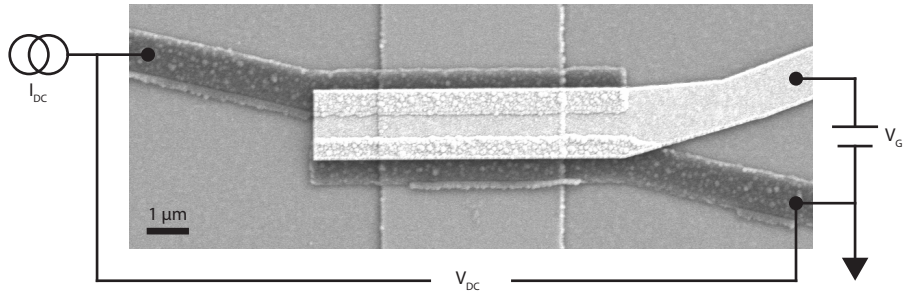

Supplementary Figure 2: A scanning electron micrograph showing the layout of the junctions. A mesa 4 microns in width was contacted by Ti/Al leads. The voltage drop V_{DC} across these leads was monitored as a function of the DC current I_{DC} flowing between them. A voltage V_G applied to a topgate was used to tune the electron density in the device.

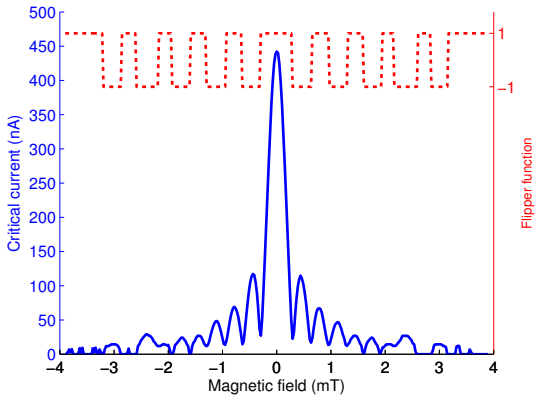

Supplementary Figure 3: Recovering the critical current phase. When the current distribution is mostly symmetric, the experimentally observed critical current envelope (blue line) approaches zero between peaks. In such cases a flipping function (red dashed line) that changes sign at each node of the envelope enables the recovery of $\mathscr{I}_C(B)$ from $I_C^{max}(B)$.

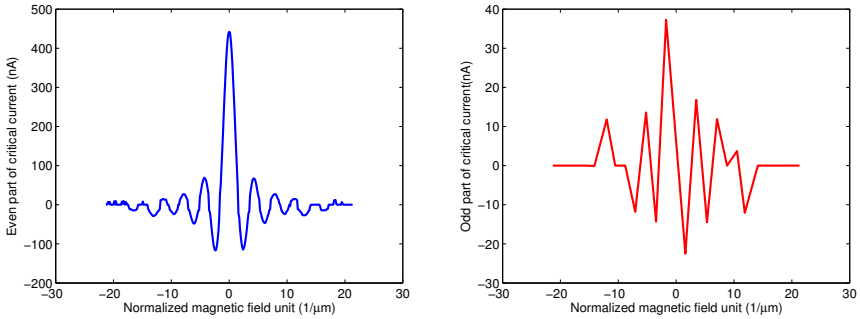

Supplementary Figure 4: Recovered complex critical current. a, The recovered critical current $I_E(\beta)$ that corresponds to the even part of the current density profile $J_E(x)$. b, The recovered critical current $I_O(\beta)$ that corresponds to the odd part of the current density profile $J_O(x)$.

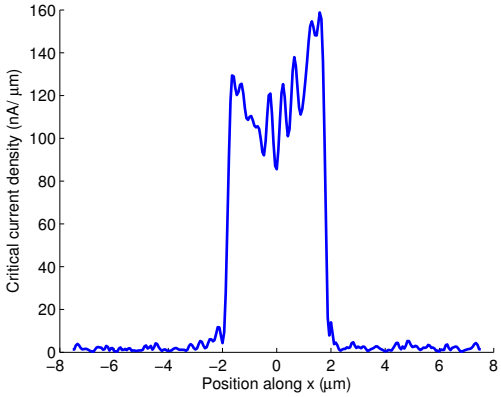

Supplementary Figure 5: The current density profile $J_S(x)$ that corresponds to the envelope in Supplementary Figure 3.

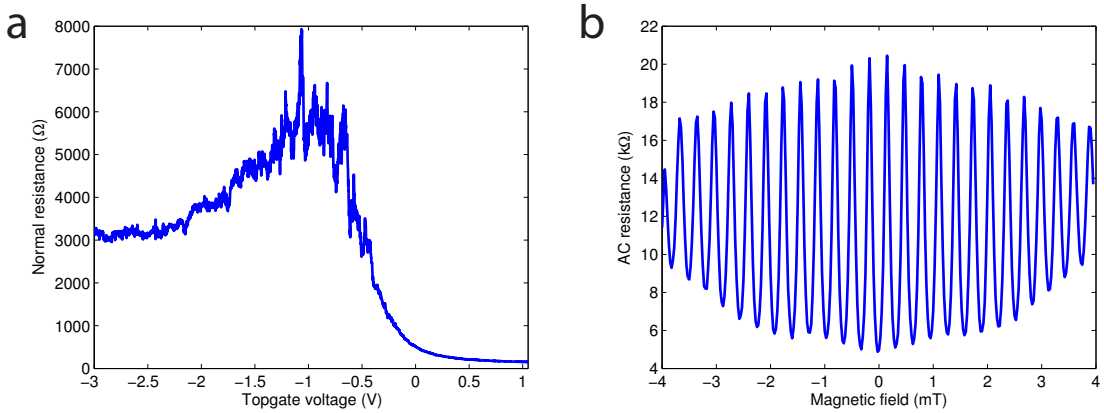

Supplementary Figure 6: Additional data for the topological junction discussed in the main text, as the carrier density in the HgTe is depleted even further. a) As a function of the topgate voltage the normal AC resistance peaks near 6-8 kΩ, consistent with the QSH effect in the presence of several additional bulk modes. b) The junction's AC resistance as a function of magnetic field, measured with the topgate voltage at $V_G = -0.7$ V and with no DC current bias. Even though the resistance minima are far from 0 Ω, the resistance oscillates with a period corresponding to $\Phi_0 = h/2e$. This periodic behavior is consistent with the superconducting interference observed at higher densities, and suggests that supercurrent transport persists well into the QSH regime.

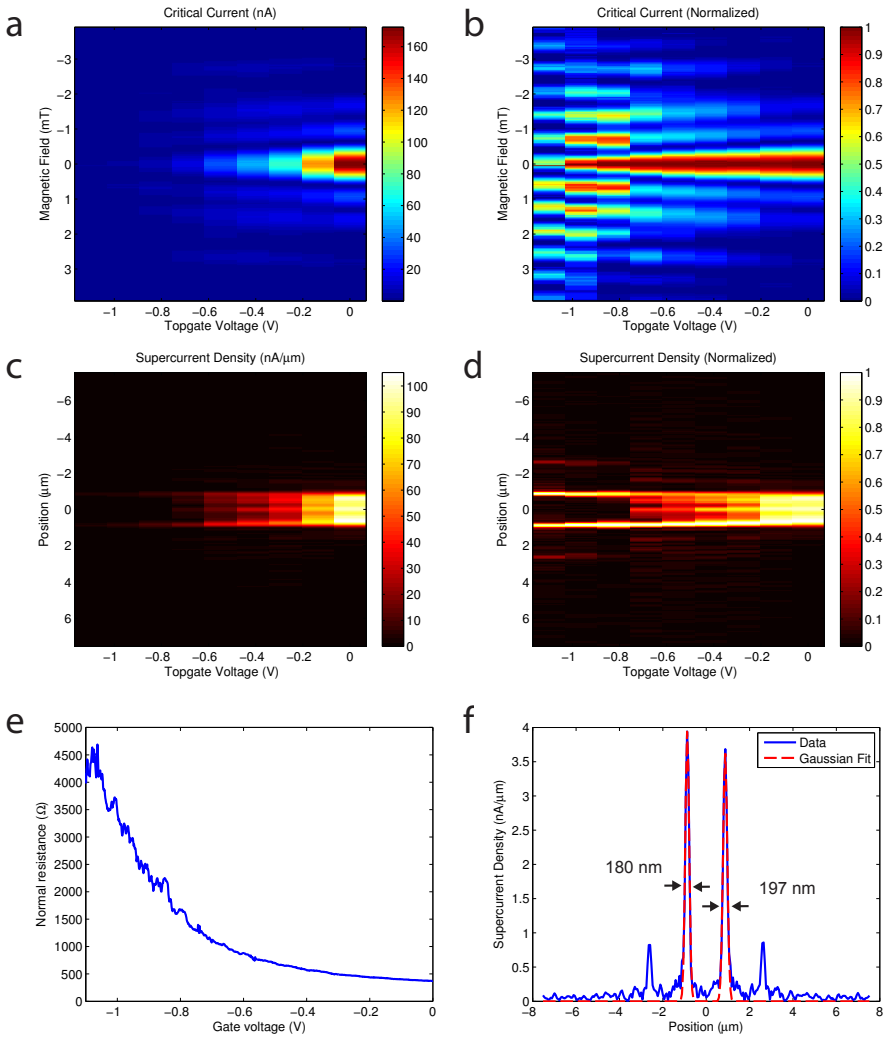

Supplementary Figure 7: Data from a Josephson junction fabricated using Wafer I, the 7.5 nm quantum well. This junction was identical to the one presented in the main text, except that the width of the mesa is 2 microns. a) A map of the critical current envelope as a function of topgate voltage shows that this device has a magnetic field period of 0.68 mT, consistent with the overall area of the device. b) After normalization the interference patterns show the evolution of this device into the QSH regime. The decay of the interference envelope over roughly 4 mT in the QSH regime is determined by the widths of the edge channels. c, d) The supercurrent density shows the confinement of supercurrent to edge modes as the bulk density is depleted. e) The normal resistance of the junction as a function of the topgate voltage. f) Edge widths extracted from the supercurrent density at the farthest negative gate voltage (-1.1 V).

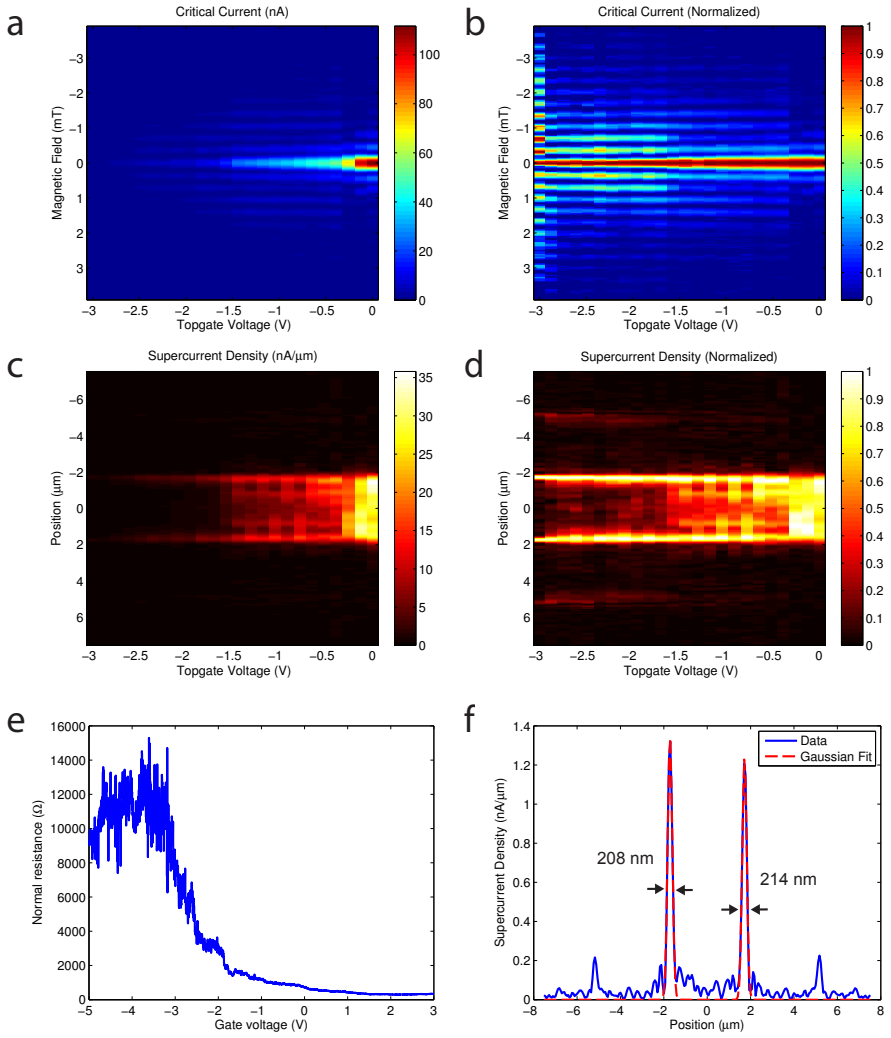

Supplementary Figure 8: Data from a Josephson junction fabricated using Wafer I, the 7.5 nm quantum well. This junction was identical to the one presented in the main text, except that the topgate was 200 nm and centered between the contacts. a,b) Consistent with other topological devices, the critical current envelope tranforms from a single-slit to a sinusoidal pattern as the density is decreased. The decay of the interference lobes is over roughly 4 mT at the most negative gate voltage. c, d) The supercurrent density shows the confinement of supercurrent to edge modes as the bulk density is depleted. e) The normal resistance of the device, extending beyond the $4,000$ ohms where the smallest supercurrents were observed. The resistance approaches the expected value for transport through two ballistic QSH edges. f) Edge widths extracted from the supercurrent density at the farthest negative gate voltage.